ACSNANO

www.acsnano.org

ARTICLE

# Quantitative Fluorescence Sensing Through Highly Autofluorescent, Scattering, and Absorbing Media Using Mobile Microscopy

Zoltán Göröcs,[†,‡,§] Yair Rivenson,[†,‡,§] Hatice Ceylan Koydemir,[†,‡,§] Derek Tseng,[†,‡,§] Tamara L. Troy,[∥] Vasiliki Demas,[∥] and Aydogan Ozcan*[,†,‡,§]

[†]Electrical Engineering Department, [‡]Bioengineering Department, and [§]California NanoSystems Institute (CNSI), University of California, Los Angeles, California 90095, United States

[∥]Verily Life Sciences, LLC, Mountain View, California 94043, United States

Supporting Information

**ABSTRACT:** **Compact and cost-effective systems for *in vivo* fluorescence and near-infrared imaging in combination with activatable reporters embedded inside the skin to sample interstitial fluid or blood can enable a variety of biomedical applications. However, the strong autofluorescence of human skin creates an obstacle for fluorescence-based sensing. Here we introduce a method for quantitative fluorescence sensing through highly autofluorescent, scattering, and absorbing media. For this, we created a compact and cost-effective fluorescence microscope weighing <40 g and used it to measure various concentrations of a fluorescent dye embedded inside a tissue phantom, which was designed to mimic the optical characteristics of human skin. We used an elliptical Gaussian beam excitation to digitally separate tissue autofluorescence from target fluorescence, although they severely overlap in both space and optical spectrum. Using ∼10-fold less excitation intensity than the safety limit for skin radiation exposure, we successfully quantified the density of the embedded fluorophores by imaging the skin phantom surface and achieved a detection limit of ∼5 × $10^5$ and ∼2.5 × $10^7$ fluorophores within ∼0.01 μL sample volume that is positioned 0.5 and 2 mm below the phantom surface, corresponding to a concentration of 105.9 pg/mL and 5.3 ng/mL, respectively. We also confirmed that this approach can track the spatial misalignments of the mobile microscope with respect to the embedded target fluorescent volume. This wearable microscopy platform might be useful for designing implantable biochemical sensors with the capability of spatial multiplexing to continuously monitor a panel of biomarkers and chronic conditions even at patients' home.**

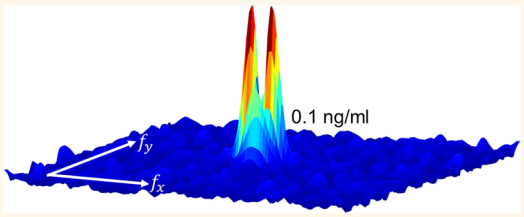


**KEYWORDS:** *fluorescent sensing through skin, skin autofluorescence, wearable imaging and sensing, mobile microscopy, wearable microscopy*

Fluorescent biomarkers have become an important tool for biotechnology since they can offer specificity and sensitivity in detecting and monitoring various biochemical reactions that are of interest for medical diagnostics and therapy and are being routinely used, *e.g.*, the detection of cancer, tracking of biomolecular dynamics of various analytes, drug delivery/release, and measurement of enzymatic reactions within their native environments.[1−15] Recently, with the emergence of highly stable and biocompatible fluorescent dyes, opportunities are created for noninvasive sensing and quantification of biomarkers through the skin. On the other hand, the detection of fluorescent objects or reactions through skin is challenging due to the presence of inherent biological fluorophores in the tissue itself. Among others, collagen, tryptophan, melanin, and nicotinamide adenine dinucleotide create a strong autofluorescence background with a broad emission bandwidth in the visible spectrum, which makes it quite difficult to detect fluorescent biomarkers or reactants through human skin.[16−18] Various methods have been implemented to investigate this challenging problem using different spectroscopy and sensing systems.[19] Some of these include ratiometric techniques that take into account the measured fluorescence emission in addition to the reflected excitation light,[20] techniques that can selectively record photons that propagate a short distance in tissue,[21,22] among other theoretical and numerical methods.[23−25] Different than these previous approaches, in this manuscript we focus on quantitative fluorescence sensing through highly autofluorescent, scattering, and absorbing media using an imaging system, *i.e.*, a wearable microscope.

**Received:** July 30, 2016
**Accepted:** September 13, 2016





DOI: 10.1021/acsnano.6b05129
*ACS Nano* XXXX, XXX, XXX−XXX

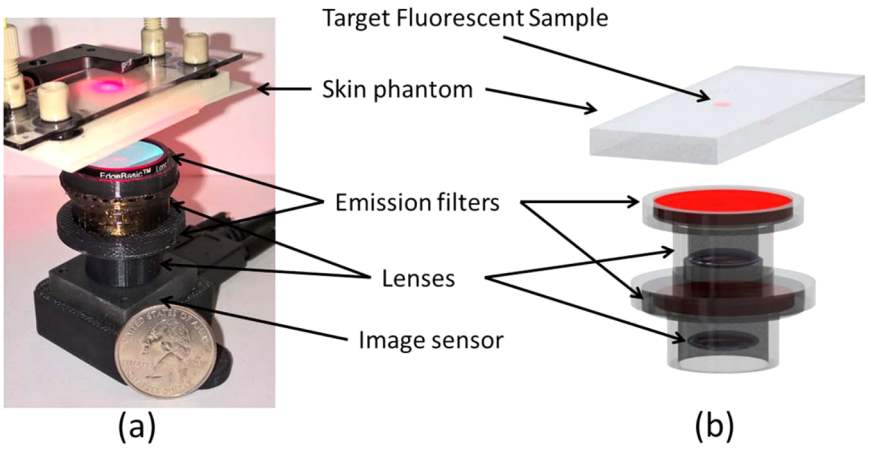


**Figure 1. (a) Photograph of the setup showing the mobile fluorescence imaging system together with the microfluidic device holding the skin tissue phantom. (b) Schematic view of the components in our mobile imaging system.**

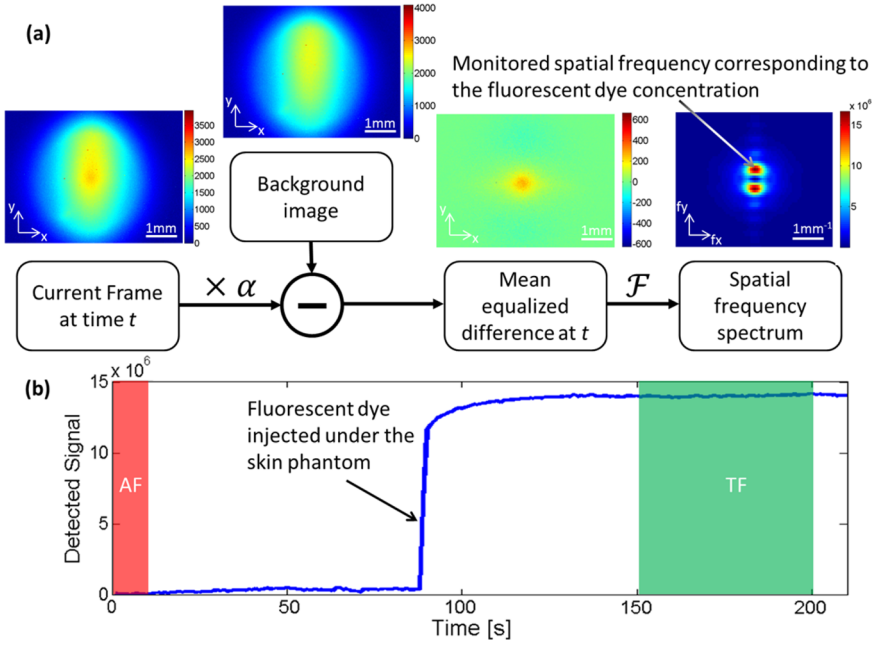


**Figure 2. (a) Processing of the acquired fluorescence images using our mobile microscope. The fluorescence intensity distribution at the skin surface corresponding to the tissue autofluorescence and the presence of the target fluorophores is imaged at a framerate of 1 fps. The first 10 frames of the measured data are averaged to provide a reference background image corresponding to the initial autofluorescence of the tissue phantom. During the successive measurements, this averaged background frame is subtracted from each fluorescence image after mean equalization. The spatial frequency spectrum of the resulting image is then calculated, and the amplitude of the frequency corresponding to the spatial differences caused by the presence of the target fluorophores is monitored. The inset images correspond to a high concentration of fluorophores for better visualization of the data processing flow. (b) The detected signal (*i.e.*, the amplitude of the monitored spatial frequency) is presented over time. The red and green highlighted zones refer to the sequence of fluorescence images used to calculate the background autofluorescence (AF) and the target fluorescence (TF) signals, respectively.**

Even though the skin's autofluorescence emission decreases toward longer excitation wavelengths,[26,27] complete spectral separation is not feasible in the visible part of the spectrum, and therefore the shot noise of the autofluorescence provides a significant limitation for subcutaneous detection of target fluorescent signals. Several approaches have been developed in recent years to overcome this obstacle, such as applying fluorescence lifetime imaging techniques for distinguishing the target fluorescence signal from tissue autofluorescence.[28] Some other techniques used to increase the target fluorescence detection sensitivity rely on taking measurements at multiple excitation and emission bands and applying spectral unmixing methods to detect the target fluorescence signal.[29,30] In one particular implementation of such techniques, the autofluorescent background was approximated using a measurement with a lower excitation wavelength to only excite the tissue and then subtracting this background measurement from a subsequent measurement taken with a wavelength that is optimized to excite the target dye.[31] While these previous approaches have shown promising results, most of them are quite expensive and hard to miniaturize in the form of a wearable imaging and sensing system, *e.g.*, patients to use at their homes. In addition to the presence of skin autofluorescence, the photobleaching of autofluorescence during the


DOI: 10.1021/acsnano.6b05129
ACS Nano XXXX, XXX, XXX−XXX

exposure of the skin to the excitation light also creates an intensity-dependent signal variation, which, in conjunction with the sensor noise and the excitation power fluctuations, adds an additional challenge to subcutaneously read and quantify target fluorescent signals or biomarkers using, *e.g.*, a wearable optical sensor or imager.

Here we demonstrate the use of a custom-designed compact and cost-effective mobile microscope (Figure 1) to measure the concentration of a target fluorescent dye that is embedded within a tissue phantom that mimics the autofluorescence, scattering, and absorption characteristics of human skin. This lightweight wearable microscope utilizes a spatial Fourier transform-based image processing method (see Figure 2) that takes advantage of the spatial modulation of the excitation beam to digitally separate the signature of the target fluorescent signal from tissue autofluorescence, although they severely overlap in space and optical spectrum. We demonstrated the success of this approach by detecting various concentrations of Alexa 647 dye, filling a sample volume of ~0.01 $\mu$L that is imaged through 0.5 and 2 mm-thick skin phantoms using our mobile fluorescence microscope. Through these phantom experiments, using the Alexa 647 dye, we achieved a detection limit of $\sim 5 \times 10^5$ and $\sim 2.5 \times 10^7$ fluorescent molecules per sample volume for the 0.5 and 2 mm-thick phantoms, respectively, both of which come very close to the shot noise limit of our system. Furthermore, we investigated the sensitivity of our mobile fluorescence microscope to lateral misalignments with respect to the embedded fluorescent sample volume and found that (1) the obtained microscopic images can be used to track the misalignment in our mobile imaging system and (2) a lateral misalignment of ~0.6 mm degrades our limit of detection by approximately 2-fold. This approach might lead to powerful techniques for reading and quantification of subcutaneous fluorescent sensors that can be integrated with various wearable and mobile optical microscope designs,[32−36] which could enable multiplexed monitoring of biomarkers through patients' skin, potentially bringing some of the point-of-care and hospital-based biomedical sensing and diagnostics tools to the home.

## RESULTS AND DISCUSSION

**Analysis of Target Fluorescence and Autofluorescence Signals.** Our excitation beam, due to its oblique illumination angle on the tissue surface, can be expressed as a 2D Gaussian signal with different widths in the $x$ and $y$ directions. This Gaussian illumination pattern excites both the skin autofluorescence and the target fluorescent sample volume, which can be expressed on the skin surface as

$$I(x, y) = I_0 \cdot e^{-2x^2/w_x^2} \cdot e^{-2y^2/w_y^2} \quad (1)$$

where $I_0$ is a constant that depends on the illumination angle and the excitation source power, and $w_x$ and $w_y$ define the beam's radius along $x$ and $y$, respectively. Note that in our experiments, due to oblique illumination, $w_x < w_y$. The autofluorescence signal on the skin surface, $I_{AF}$, that is imaged by our microscope and its emission filters will depend on the photobleaching rate of the skin tissue and can be approximated as

$$I_{AF}(x, y, t) = u(\hat{I}(x, y, z))e^{\{(-k_0 u(\hat{I}(x,y,z))t)^\beta\}} \quad (2)$$

where the exponential coefficient $\beta \sim 1$, $k_0$ is a decay coefficient that is inversely proportional to the density/concentration of autofluorescent molecules inside tissue, $t$ refers to time, and $u(\hat{I}(x,y,z))$ is the 2D autofluorescence emission intensity *at the skin surface* that is assumed to be a monotonic and smooth function of the 3D excitation intensity, $\hat{I}(x,y,z)$, that is scattered within the tissue volume.[31,32]

We can approximate:

$$u(\hat{I}(x, y, z)) = A(x, y) \cdot e^{\{-2x^2/\sigma_{AFx}^2 - 2y^2/\sigma_{AFy}^2\}}$$

where $\sigma_{AFx} > w_x$ and $\sigma_{AFy} > w_y$ due to scattering and spreading of both the excitation light as well as the autofluorescence signal in tissue, and $A(x,y) = A_0 + a(x,y)$ represents *small amplitude* variations due to spatial nonuniformities of the *tissue scattering, absorption, and autofluorescence* properties, with mean$\{A(x,y)\} = A_0$ and $A_0 \gg |a|$. With $\beta \sim 1$, the autofluorescence signal that is imaged at the skin surface can be written as

$$\begin{aligned} I_{AF}(x, y, t) &= (A(x, y) \cdot e^{-2x^2/\sigma_{AFx}^2} \cdot e^{-2y^2/\sigma_{AFy}^2} \\ &\quad \cdot e^{-k_0 A(x,y) \exp[-2x^2/\sigma_{AFx}^2] \exp[-2y^2/\sigma_{AFy}^2] t}) \otimes \mathrm{PSF}_{mic}(x, y) \\ &\approx A_0 \cdot e^{-2x^2/\sigma_{AFx}^2} \cdot e^{-2y^2/\sigma_{AFy}^2} \cdot e^{-k_0 A_0 \exp[-2x^2/\sigma_{AFx}^2] \exp[-2y^2/\sigma_{AFy}^2] t} \end{aligned} \quad (3)$$

where $\otimes$ refers to the spatial convolution operation. In eq 3, we assumed that the point spread function (PSF) of our fluorescence microscope, $\mathrm{PSF}_{mic}(x,y)$, is (1) much narrower compared to $\sigma_{AFx}$ and $\sigma_{AFy}$ and accordingly acts like a Dirac-delta function in space and (2) broader compared to the scale of the spatial variations observed in $a(x,y)$.

It is evident from eq 3 that the impact of tissue photobleaching would be more apparent around the beam's center (where the intensity is highest), and it reduces as we move away from the center. *Stated differently, the photobleaching process introduces a strong spatial modulation to the autofluorescence signal, $I_{AF}(x,y,t)$, in addition to a temporal modulation.*

On the other hand, the impact of the photobleaching process is quite different for the target fluorescent (TF) signal that is imaged on the skin surface, $I_{TF}(x,y,t)$. In fact, since the spatial width of the target fluorescent sample embedded within the tissue/skin is much narrower compared to $\sigma_{AFx}$ and $\sigma_{AFy}$, the spatial variation of $I_{TF}(x,y,t)$ due to photobleaching can be ignored compared to $I_{AF}(x,y,t)$. *In other words, the photobleaching process mainly introduces a temporal modulation to $I_{TF}(x,y,t)$,rather than a spatial modulation.*

To expand on this last statement, let us denote the fluorophore distribution inside the *small* and *thin* sample volume as $c(x,y)$. Compared to the spatial widths of $I_{AF}(x,y,t)$ and the excitation beam profile at the sample depth (*i.e.*, $K(x,y)$) one can write $c(x,y) \approx c_o\delta(x,y)$, where $c_o$ is a constant. This is a reasonable assumption for our experiments since the fluorescent reservoir width is ~0.5 mm, which is much smaller compared to $\sigma_{AFx}$ and $\sigma_{AFy}$ as well as the spatial spread of the excitation beam at the sample depth, even for a smaller phantom depth of 0.5 mm. Then, using $\beta \sim 1$, the spatiotemporal modulation term for the target fluorescent signal can be expressed as[37,38] $K(x,y) \cdot c(x,y) \cdot e^{-k_0' K(x,y) t}$ where $k_0'$ is another decay constant that is in general a function of $c_o$ especially for low fluorophore concentrations: $K(x, y) = [I_0 \cdot e^{-2x^2/w_x^2} \cdot e^{-2y^2/w_y^2}] \otimes \mathrm{PSF}_{T,\lambda_{ex}}(x, y)$ and $\mathrm{PSF}_{T,\lambda_{ex}}(x,y)$ is the average incoherent point spread function that is introduced by the tissue scattering and absorption that the excitation beam ($\lambda_{ex}$) faces for a skin thickness of $T$, *i.e.*, $c(x,y)$ lies below the surface of the skin by an amount that is


DOI: 10.1021/acsnano.6b05129
ACS Nano XXXX, XXX, XXX−XXX

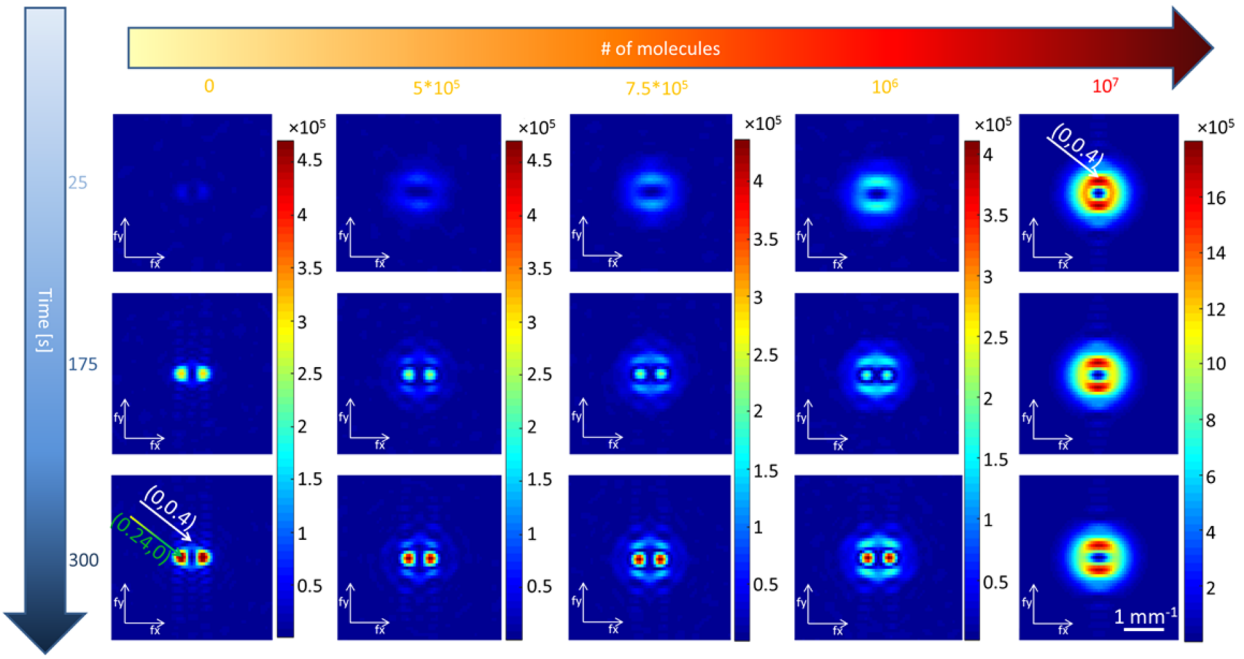


**Figure 3. Simulation results for $|G(f_x,f_y,t)|$ corresponding to our fluorescence imaging conditions for various target fluorophore concentrations and time points. For a given target dye concentration that is constantly replenished, as time progresses, the amplitude of the monitored spatial frequency on the $f_y$ axis (white arrow) remains approximately constant. As expected, for a given $t$ value, the amplitude of the monitored spatial frequency increases with the increasing concentration of the target dye. $T$ = 0.5 mm. The origin is at the center of each spatial frequency image.**

given by $T$ (0.5 mm or 2 mm in our experiments). Because $K(x,y)$ is much broader than $c(x,y)$, we have

$$K(x,y)\cdot c(x,y)\cdot e^{-k_0' K(x,y)t} \approx K_0\cdot c(x,y)\cdot P(t) \quad (4)$$

where $K_0 = K(x = 0, y = 0)$ is a constant and $P(t) = e^{-k_0' K_0 t}$ represents the temporal modulation that the photobleaching process introduces in $I_{TF}(x,y,t)$.

Based on eq 4, the image of the fluorescent intensity distribution at the surface of the skin due to the target embedded fluorophores can be expressed as

$$\begin{aligned} I_{TF}(x,y,t) &\approx P(t)\cdot[\{K_0\cdot c(x,y)\} \otimes \mathrm{PSF}_{T,\lambda_{em}}(x,y)] \otimes \mathrm{PSF}_{mic}(x,y) \\ &\approx K_0\cdot P(t)\cdot[c(x,y) \otimes \mathrm{PSF}_{T,\lambda_{em}}(x,y)] \end{aligned} \quad (5)$$

where $\mathrm{PSF}_{T,\lambda_{em}}(x,y)$ is the average incoherent point spread function that is introduced by tissue scattering and absorption corresponding to the emission wavelength ($\lambda_{em}$), for a given skin thickness of $T$. Note that, similar to eq 3, the incoherent PSF that is introduced by our fluorescence microscope is much narrower in space compared to tissue-induced PSFs (for $T \geq$ 0.5 mm) and therefore $\mathrm{PSF}_{T,\lambda_{em}}(x,y) \otimes \mathrm{PSF}_{mic}(x,y) \approx \mathrm{PSF}_{T,\lambda_{em}}(x,y)$. Assuming that the average incoherent point spread function due to the presence of tissue has a Gaussian distribution,[39] *i.e.*, $\mathrm{PSF}_{T,\lambda}(x,y) = \alpha_{T,\lambda}\cdot e^{\{-2(x^2+y^2)/\sigma_{T,\lambda}^2\}}$, eq 5 can then be written as

$$I_{TF}(x,y,t) \approx K_0'\cdot P(t)\cdot[c(x,y) \otimes (e^{\{-2(x^2+y^2)/\sigma_{T,\lambda_{em}}^2\}})] \quad (6)$$

where $K_0' = K_0\cdot\alpha_{T,\lambda_{em}}$. Note that eq 6 is valid after the fluorescent sample has been introduced or embedded into the tissue, which in our notation covers $t > 0$.

Both $I_{TF}$ and $I_{AF}$ spectrally and spatially overlap during our imaging experiments, *i.e.*, $I_{mic}(x,y,t) = I_{TF}(x,y,t) + I_{AF}(x,y,t)$. By comparing eqs 3 and 6, we can see that a major difference between these two signals is that the photobleaching process introduces a strong spatiotemporal modulation in $I_{AF}$, whereas it only introduces a temporal modulation, $P(t)$, in $I_{TF}$. This feature helps us to separate these two signals from each other using their different spatial distributions, imaged through the surface of the skin using our mobile microscope. For this end, we acquire a *background image* at $t = 0$ (see Figure 2) without the presence or implantation of the target fluorophores in the sample volume, *i.e.*, $I_{back} = I_{mic}(x,y,t = 0) = I_{AF}(x,y,t = 0)$. Then, as illustrated in Figure 2, for any microscopic image acquired at $t > 0$, we calculate:

$$\begin{aligned} g(x,y,t) &= \alpha(t)\cdot I_{mic}(x,y,t) - I_{back} = \alpha(t)\cdot I_{TF}(x,y,t) \\ &+ \alpha(t)\cdot I_{AF}(x,y,t) - I_{AF}(x,y,t = 0) \end{aligned} \quad (7)$$

where $\alpha(t) = \mathrm{mean}\{I_{back}\}/\mathrm{mean}\{I_{mic}(x,y,t)\}$. The function of $\alpha(t)$ is to equalize the signal means, which also removes the effect of potential illumination fluctuations. Following this mean equalization procedure, we have $\mathrm{mean}\{g(x,y,t)\} = 0$, and the nominal value of $\alpha(t)$ in our experiments is ~1.01.

As a function of the target dye concentration and time, $I_{TF}(x,y,t)$ will cast its signature in the form of a spatial distribution change in $g(x,y,t)$, and therefore one of the best ways to monitor the target fluorescent signal or its concentration would be through a 2D spatial Fourier transform ($\mathcal{F}$) of $g(x,y,t)$, *i.e.*, $G(f_x, f_y, t) = \mathcal{F}(g(x,y,t))$. To better visualize and investigate this, based on the mathematical formalism and the equations that we outlined above, we created a numerical simulation framework to understand the evolution of the spatial frequencies of $g(x,y,t)$ as a function of both the target fluorescent molecule concentration as well as time. These



DOI: 10.1021/acsnano.6b05129
ACS Nano XXXX, XXX, XXX−XXX

simulations results, as summarized in Figure 3, illustrate that the amplitude of $G(f_x,f_y,t)$ exhibits some characteristic peaks; the amplitudes and specific locations of these peaks depend on the illumination profile, tissue photobleaching as well as the target dye concentration and its spatial function, $c(x,y)$. In our simulation results (Figure 3), two of these peaks that are approximately centered at $(f_x,f_y) = (\pm 0.24\ \text{mm}^{-1}, 0)$ very well represent the behavior of the autofluorescence signal for a background image or for images acquired at very low target fluorophore concentrations, whereas the other two peaks at $(f_x,f_y) = (0, \pm 0.4\ \text{mm}^{-1})$ can be used to track the target fluorescent signal defined by $c(x,y)$. As desired, Figure 3 illustrates that the amplitude of this target spatial frequency $(0, \pm 0.4\ \text{mm}^{-1})$ at a given $t$ value gets larger as a function of the concentration of the fluorophores within the target sample volume; and for a given target dye concentration that is constantly replenished, as time progresses, the amplitude of the same target spatial frequency remains approximately constant (in addition to Figure 3, also see Figure 2b for an independent experimental confirmation of this). These simulations assumed the same range of physical parameters as we used in our experiments (see Table 1), and overall, they provide very good agreement to our experimental results, which are summarized in Figure 4. In these simulations and experimental results (Figures 3 and 4), we have $w_x < w_y$ due to our oblique illumination angle (~70°). If one switches the illumination angle such that $w_y < w_x$, the spatial frequency peaks that represent background autofluorescence and target fluorescence signals will also switch or rotate 90° in the $f_x$–$f_y$ plane.

**Table 1. System Parameters Used in Our Numerical Simulations**

| $\sigma_{AFx}$ (mm) | $\sigma_{AFy}$ (mm) | $c(x,y)$ (mm) | $c_o$ | $\sigma_{em}$ (mm) | $T$ (mm) | $K_0'$ ($\Theta$ = 70°) |
|---|---|---|---|---|---|---|
| 2.2 | 6.2 | Ø 0.5 | no. of molecules, as reported in each figure | 0.62 | 0.5 | 0.18 |

We further investigated the effect of the incidence angle, thus the ellipticity of our Gaussian illumination profile on the performance of this fluorescence imaging system. Using a laser diode with an oblique illumination angle is especially *practical* in a wearable system, as it makes the imaging setup extremely compact while also avoiding a *direct* reflection of the excitation beam off the skin surface to enter into the wearable microscope. In addition to these advantages, as demonstrated in Figure 4 this oblique illumination angle also helps us to separate the contributions of the tissue autofluorescence from the target fluorescent signal in the spatial frequency domain by perturbing the 2D functional form of the autofluorescence signal at the skin surface to be different than the functional form of the target fluorescent signal that is imaged through our mobile microscope (*i.e.*, eqs 3 *vs* 6). Figure 5 further illustrates that oblique illumination angles greatly reduce the impact of the autofluorescence signal, measured at the spatial frequency that is used to track the presence of the target fluorescent sample (*i.e.*, $(f_x,f_y) = (0, \pm 0.4\ \text{mm}^{-1})$ for our choice of $c(x,y)$). However, further increasing the incidence angle over ~70° would provide a diminishing return and more importantly

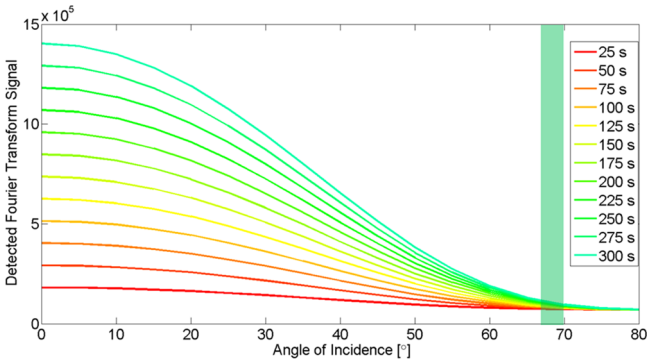


**Figure 5. Simulation results illustrate, as a function of the illumination angle of the excitation beam, the magnitude of the Fourier transform of the tissue autofluorescence signal (without any target fluorophore present) at the same spatial frequency that is normally used to track the target fluorescence signal. Increasing the illumination angle minimizes the contribution of the autofluorescence signal at the target spatial frequency. In our experiments, we used an illumination angle that is approximately labeled with the green transparent bar on the plot. $T$ = 0.5 mm.**

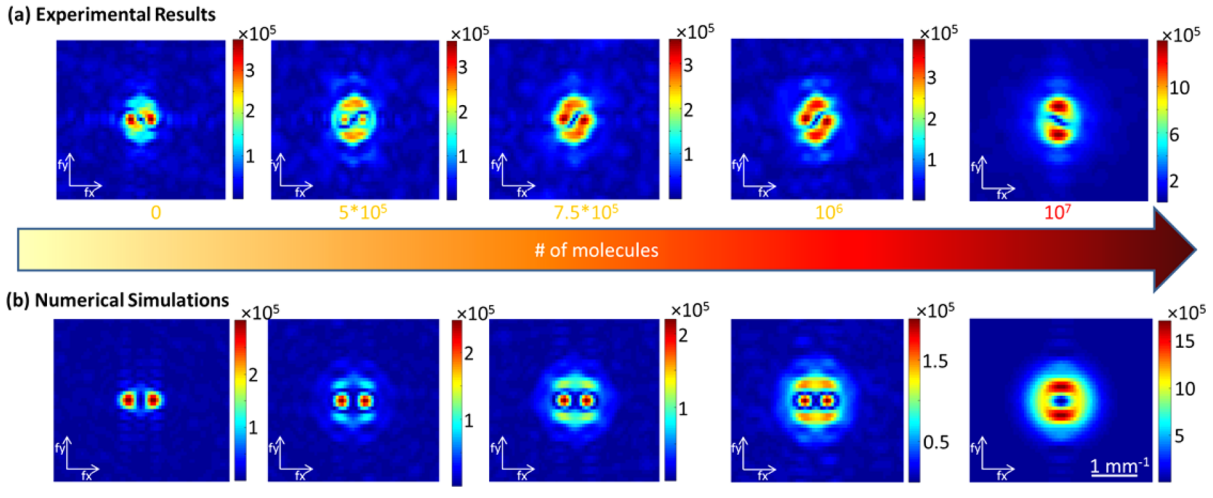


**Figure 4. A comparison of our experimental results (a) and numerical simulations for $|G(f_x,f_y,t = 175\ \text{s})|$ as a function of the target dye concentration. $T$ = 0.5 mm. The colorbar in each image was optimized to maximize the visibility of the image at that particular concentration. The origin is at the center of each spatial frequency image.**



DOI: 10.1021/acsnano.6b05129
ACS Nano XXXX, XXX, XXX–XXX

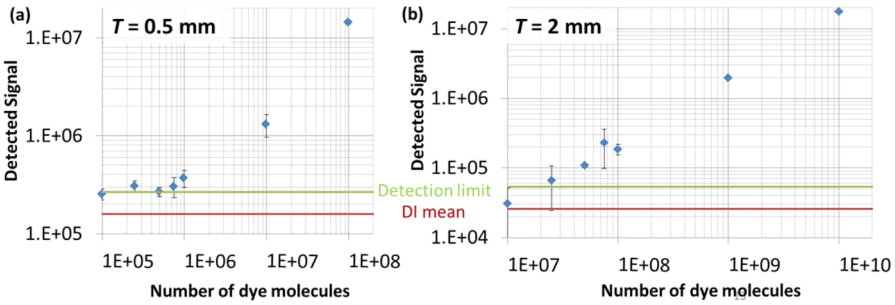


**Figure 6. Average and the standard deviation of the detected signal for various dye concentrations for $T$ = (a) 0.5 and (b) 2 mm tissue phantom thicknesses. The detection limit is set to be the mean plus 3 times the standard deviation of the DI water measurements. For $T$ = 0.5 mm our detection limit is ~5 × $10^5$ fluorophores per 0.01 $\mu$L sample volume, while for $T$ = 2 mm, it increases to ~2.5 × $10^7$ fluorophores for the same volume.**

rapidly reduce the intensity of the excitation beam on the skin surface for a given power level of the illumination source and therefore waste the available photon budget for the limited field-of-view (FOV) of a wearable imaging system.

**Investigation of the Limit of Detection, Repeatability, and Alignment Sensitivity of the Mobile Microscope.** After establishing the mathematical background of our approach and its experimental validation, next we investigated how it performs for the detection of low concentrations of fluorescent dyes in the presence of a spectrally overlapping and time-dependent autofluorescent and scattering background. The key aspect of our Fourier transform-based method, as detailed in the previous subsection, is to utilize a nonuniform excitation profile using, *e.g.*, an oblique illumination angle. The use of a simple elliptical Gaussian intensity profile for the excitation beam allows us to modulate the spatial frequency distribution of the tissue autofluorescence response and separate it from the target fluorescence response embedded within the tissue.

Using our mobile fluorescence microscope shown in Figure 1, we measured the limit of detection and the linearity of our target signal extracted using our Fourier transform-based processing approach by imaging a sample well of 0.01 $\mu$L volume, filled with various concentrations of Alexa 647 dye through 0.5 and 2 mm-thick skin tissue phantoms (see Figure 6). The limit of detection was determined by comparing our measurements for different concentrations of fluorophores to the mean plus three times the standard deviation of the measurements made using pure DI water. The results revealed that the limit of detection for a well-aligned imaging system using our mobile microscope is 5 × $10^5$ Alexa 647 dye molecules per 0.01 $\mu$L sample volume that is embedded within the 0.5 mm-thick tissue phantom, which corresponds to a dye concentration of 105.9 pg/mL. As expected, the limit of detection for the 2 mm-thick skin phantom degraded due to the increased light absorption, scattering, and autofluorescence inside the thicker tissue phantom and was measured as ~2.5 × $10^7$ Alexa 647 dye molecules per 0.01 $\mu$L sample volume, corresponding to a fluorophore concentration of 5.3 ng/mL.

Next we investigated the tolerance of our imaging system to spatial misalignments, as one would expect to have in any wearable imaging and sensing system. For this purpose, we introduced 0.6 mm lateral misalignment within the FOV of our mobile microscope with respect to the embedded fluorescent sample volume, which is normally positioned to be at the center of our FOV. As illustrated in Figures 7 and 8, due to this lateral misalignment, our limit of detection degraded approximately by

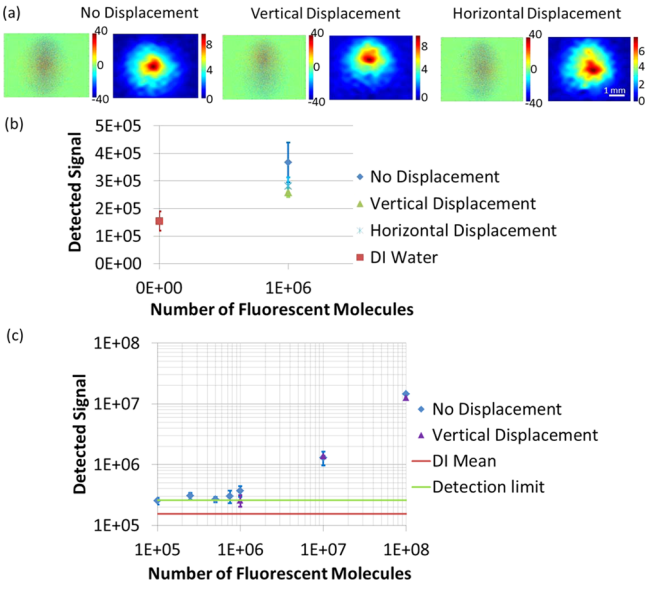


**Figure 7. Tolerance of the mobile fluorescence microscope-based sensing system to 0.6 mm horizontal and vertical misalignments for $T$ = 0.5 mm. (a) Measured fluorescent responses due to the target dye (after background subtraction) are shown for well aligned, vertically misaligned, and horizontally misaligned microscopes. In each case, the left image is before, and the right image is after the noise reduction by a low pass spatial filter. High-intensity spot of each filtered image corresponds to the location of the embedded fluorescent sample, tracking the amount of misalignment in the imaging system. (b) The change in the detected signal for horizontal and vertical misalignments (using ~$10^6$ fluorophores per sample volume, 0.01 $\mu$L). (c) Measurements for various fluorescent dye concentrations with and without 0.6 mm vertical misalignment. The linearity of the detected signal *vs* the target concentration is preserved.**

a factor of 2 for both the 0.5 and 2 mm-thick tissue phantoms. For a tightly placed wearable microscope, this level of misalignment can be tolerated. In fact, for a given misaligned imaging system, the location of the embedded fluorescent sample beneath the tissue surface can be independently inferred by low-pass filtering of the background subtracted image frames to remove the high-frequency noise of the image sensor (*e.g.*, see Figures 7a and 8a). Based on these filtered images, one can periodically estimate the amount of misalignment in the wearable imager and adaptively correct it through, *e.g.*, steering of the excitation beam. The large FOV of our mobile fluorescence microscope design with a diameter of ~4 mm


DOI: 10.1021/acsnano.6b05129
ACS Nano XXXX, XXX, XXX−XXX

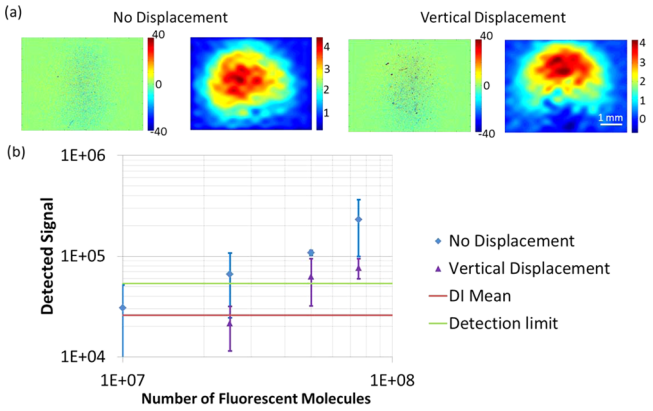


**Figure 8. Same as in Figure 7, except for 0.6 mm vertical misalignment using ~7.5 × $10^7$ fluorophores per sample volume (0.01 $\mu$L) and $T$ = 2 mm. The thicker skin tissue phantom causes a wider distribution of the fluorescence signal, which still tracks the misalignment/displacement in the imaging system as shown in (a).**

permits the use of such an adaptive correction procedure by simple steering of the excitation beam, even by a few degrees through *e.g.*, a microelectromechanical system (MEMS)-based mirror that can be integrated into the excitation beam path. This would mean that a given misalignment of the wearable imaging system can be estimated and accordingly corrected, and the system can be realigned through such an adaptive approach by making use of the spatial redundancy of our large imaging FOV compared to the small embedded sample/sensor area.

**Future Design Considerations and Challenges toward an Ultrathin Wearable Microscopy and Sensing System.** In a wearable optical sensor design, compactness, lightweight, and robustness are important requirements. Mostly driven by the consumer electronics industry (in particular mobile phone manufacturers), camera modules are becoming increasingly more compact and thinner; however lens-based imaging systems inherently have a physical limit on their minimal size. As an alternative to lens-based designs, lens-free imaging technologies have already been developed[40,41] for computational microscopy and sensing applications[42−44] aiming to provide thinner, more compact, wider FOV and more cost-effective imagers compared to their lens-based counterparts, and here we will discuss the design considerations as well as potential advantages and disadvantages of lens-free imaging techniques toward the design of next generation wearable sensor platforms.

One potential candidate to replace lens-based image relay systems for a wearable sensor design involves the use of a fiber optic faceplate in a lens-free on-chip imaging geometry.[42,44] Each faceplate consists of thousands of optical fibers bonded together in a bundle with a light absorbing material placed in between them. Its function is to transmit the intensity distribution on one of its surfaces (*e.g.*, in contact with the skin) to the opposite surface, where we can directly place an optoelectronic sensor array, *e.g.*, a CMOS imager chip without any alignment or focusing needed, forming a lens-free contact imaging and sensing system on the skin surface.

Using such a fiber-optic faceplate-based lens-free on-chip microscope design for fluorescence imaging and sensing applications creates opportunities to minimize the thickness and weight of the wearable microscopic sensor while also significantly increasing the imaging FOV; for example, an imager thickness of <0.5−1 cm, a device weight of <10−20 g, and a FOV of >20−30 $mm^2$ can be achieved using this on-chip contact microscopy design. However, there are also challenges that need to be addressed. As in any fluorescence imaging system, one needs to provide the excitation to the sample and then filter the excitation light out to measure the target fluorescent signal. Since the faceplate forms a contact imaging system, delivering the excitation light onto the skin is less straightforward due to the lack of space between the faceplate and the skin. Excitation light can potentially be provided right next to the faceplate, however this would also limit the usable FOV of the wearable sensor as the excitation light would need to travel within the skin to reach the target sample volume under the faceplate. In an alternative design (see Supplementary Figure S1), the excitation light can also be provided by channeling it through the fibers of the same faceplate by, *e.g.*, integrating an array of laser diodes within the wearable sensor assembly, coupling the excitation light through the other side of the faceplate without blocking the FOV of the imager chip. In both of these cases, a relatively small area on the skin surface will be illuminated by the excitation light, and therefore, one needs to be careful about the skin exposure safety limits since higher excitation intensities would be needed to efficiently excite the target sample volume embedded in the skin.

In addition to providing a compact, thin, and wide-field imager design, fiber optic faceplates possess an additional advantage as they can be manufactured to reach a numerical aperture (NA) of ~1, providing an excellent light collection efficiency at the areas filled by the fiber cores. The parts of the faceplate volume occupied by the cladding and the stray light absorber (*i.e.*, the extramural absorption, EMA) material will not effectively transmit light, thus the maximum possible transmission at the fluorescent emission band is limited by the fill factor of the faceplate (typically *e.g.*, 70−80%). One must also carefully consider the potential autofluorescence of the utilized absorptive materials in the faceplate design to avoid sensitivity loss for the wearable system.

In addition to the efficient delivery of the excitation beam into the sample volume, the design of emission filter is equally important for high-quality fluorescence sensing and imaging. Absorption-based filter coatings have been demonstrated to work well with lens-free fiber-optic faceplate-based fluorescence sensing systems.[42−44] However, the edge steepness of the transmission spectra of absorptive materials is in general lower than their thin-film counterparts, and therefore in a lens-free design, it is advantageous to select fluorophores with a relatively wide spectral gap between their absorption and emission maxima. Also, the transmittance efficiency of absorption-based filters in the emission band of a target fluorophore is generally lower, especially at high optical densities (*e.g.*, OD6+) which would be required for a wearable sensor due to, *e.g.*, the backscattered excitation light from the skin surface.

Thin-film-based filter coatings can overcome some of the above-discussed shortcomings of absorption filters, however, they also introduce their own challenges. Due to the spectral shift of thin-film filters at increased incidence angles, one must limit the NA and therefore the light collection efficiency of the faceplate, to prohibit the light passing through the filter coating to couple into the fibers of the faceplate. These rays, however, can still propagate as cladding modes in the faceplate, thus additional EMA material is necessary, and potentially the overall thickness of the faceplate would need to be increased to reach the required optical density for the rejection of the


DOI: 10.1021/acsnano.6b05129
ACS Nano XXXX, XXX, XXX−XXX

excitation light. The angular dependence of the transmission spectrum of the thin-film filter can especially become a major limiting factor for fluorophores, where the excitation and the emission peaks are close to each other, since it can severely limit the maximum NA of the faceplate, or otherwise the cut-on wavelength of the emission filter will need to be shifted toward higher wavelengths resulting in a loss of detection sensitivity at low emission angles.

Another parameter to consider when designing a fiber-optic faceplate-based lens-free fluorescent imaging system on a chip is the bond between the faceplate and the sensor chip surfaces. The pixel size of the sensor chip and the fiber optic array orientation of the faceplate should be chosen to avoid aliasing related spatial artifacts arising from the two periodic patterns. Typically, microlenses are also employed on CMOS image sensor chips to increase the sensitivity of these devices for light rays arriving at higher incidence angles. However, their cutoff angle is well below an NA of 1 in air, which also needs to be taken into account when choosing the NA of the faceplate. Furthermore, for smaller pixel size sensors that are especially employed in mobile phone cameras, the microlens array distribution on the image sensor chip is specially designed in conjunction with the lens of the camera assembly, such that the microlenses are laterally shifted from the center position of the pixel area toward the edges of the sensor FOV in order to provide better sensitivity at higher chief ray angles. Using these types of image sensors can yield loss of sensitivity near the edges of the FOV, when they are coupled to a faceplate with a uniform angular emission across the entire FOV. Therefore, for a wearable fluorescence imaging platform, one must carefully consider and choose the image sensor chip together with the properties of the fiber optic faceplate, the filter coating, as well as the target fluorescent dye spectrum in order to exploit the potential advantages of such compact, thin, and wide-field lens-free imager designs for wearable sensor applications.

## CONCLUSIONS

In this work, we demonstrated the design of a compact and cost-effective mobile microscope for sensing small quantities of fluorescent dye molecules in the visible part of the spectrum through a highly autofluorescent, scattering, and absorbing phantom that mimics human skin. Using this mobile microscopy platform along with a spatial frequency-based signal processing scheme, we achieved a detection limit of $\sim 5 \times 10^5$ and $\sim 2.5 \times 10^7$ Alexa 647 fluorescent molecules within a sample volume of $\sim 0.01\ \mu$L that is positioned 0.5 and 2 mm below the surface of a skin tissue phantom, which correspond to a dye concentration of 105.9 pg/mL and 5.3 ng/mL, respectively. We also demonstrated that this approach can be used to track the spatial misalignments of the mobile microscope with respect to the location of the embedded target fluorescent sample and that a lateral misalignment of $\sim 0.6$ mm degrades our limit of detection approximately by 2-fold. All of these experimental results were achieved using an excitation intensity level that is approximately an order of magnitude below the safe long-term exposure limit of the human skin. With rapid advances in optical sensor technologies, we believe that the presented approach might prove useful for designing fluorescence sensors that can be read subcutaneously using wearable microscopes, enabling various powerful device concepts for multiplexed, continuous monitoring, and quantification of a panel of biomarkers and chronic conditions at home or at point-of-care settings.

## METHODS

**Optical Imaging Setup.** Our optical setup consists of four main parts: the excitation source, the image relay lenses, the emission filters, and the image sensor chip. All the imaging components are enclosed within a custom-designed 3D printed opto−mechanical interface, which weighs <40 g (see Figure 1). The excitation light is provided by a laser diode (Thorlabs LP642-FS20) at 642 nm. The output of the laser is collimated to have a beam diameter of ∼4.4 mm, and the Gaussian beam of this excitation source illuminates the skin phantom at an incidence angle of ∼70°. The average intensity of the beam is 0.24 mW/mm$^2$, which is ∼8-fold smaller than the safe long-term exposure limit for human skin.[45] The image of the object is relayed by a pair of lenses (Evetar M13B1618IR) achieving a magnification of 0.85×. The excitation light is filtered by a pair of thin-film filters (Chroma ET700/75m and Semrock BLP01−664R-25), one placed between the lenses and the other one placed before the front lens, respectively. These two filters were selected by considering the angle-dependent transmission characteristics of thin-film filters in conjunction with the properties of the lenses in our design. In our compact wearable imaging geometry, the lenses are positioned in close proximity to each other to maximize the FOV of the system and reduce vignetting effects. Due to their short focal lengths and low f-numbers, this dual filter geometry was utilized to block the excitation light from reaching the image sensor chip regardless of the sample position within the FOV, while still allowing the majority of the emission spectrum of the target dye to pass. The fluorescence image of the skin phantom is captured using a board level CMOS camera (Basler Dart daA1280−54um). The diameter of the FOV of our imaging system is ∼4 mm.

**Skin Phantom.** The tested skin phantom samples were fabricated at Verily to mimic the autofluorescence, scattering, and absorbing characteristics of human skin[46] at our excitation and emission wavelengths. The phantom substrate was made out of PDMS (Sylgard(R) 184 Silicone Elastomer Kit), and the scattering and absorbance properties were adjusted by adding $TiO_2$ particles (<5 $\mu$m in diameter, from Sigma-Aldrich, SKU-248576-100G) and carbon black (Sigma-Aldrich, 699632-25g), respectively.[47] To mimic the autofluorescence characteristics of Caucasian human skin, specifically the forearm, Disperse Red (Sigma-Aldrich, 344206-5G) was used as the fluorescent dye embedded within the phantom. The absorption ($\mu_a$) and isotropic scattering ($\mu_s'$) coefficients, the anisotropy ($g$), and the refractive index ($n$) of the skin phantom for the excitation and detection wavelengths utilized in our fluorescence imaging experiments are summarized in Table 2. The isotropic scattering and absorption coefficients were measured using the double integrating sphere[48] technique and the inverse adding-doubling[49] method, and the anisotropy was calculated using the Mie theory.[50] Each phantom is bonded on the top of a microfluidic channel, containing a cylindrical reservoir with a diameter of 0.5 mm and a sample volume of ∼0.01 $\mu$L connected to a microfluidic system with an inlet and outlet, which are used to introduce varying concentrations of fluorophores into the sample volume. In our experiments we used 0.5 and 2 mm-thick skin phantoms to evaluate the effect of tissue thickness on our measurement sensitivity.

**Table 2. Optical Properties of the Skin Tissue Phantom That We Used in This Work**

| $\lambda$ (nm) | $\mu_a$ (1/mm) | $\mu_s'$ (1/mm) | $g$ | $n$ |
|---|---|---|---|---|
| 650 | 0.06 | 2.61 | 0.7 | 1.42 |
| 700 | 0.06 | 2.42 | 0.7 | 1.42 |

**Measurement Workflow.** We prepared various concentrations of the target fluorescent dye (Alexa 647) for our measurements. Alexa 647 was selected in our experiments as it can be excited by and emits at the far-red part of the electromagnetic spectrum, where the skin's autofluorescence and absorption are both reduced compared to lower wavelengths. This fluorescent molecule also has a relatively high quantum efficiency of ∼0.33 which is important due to the limited


DOI: 10.1021/acsnano.6b05129
ACS Nano XXXX, XXX, XXX−XXX

excitation photon budget that is enforced by the human skin radiation exposure safety limits. Furthermore, it can be efficiently excited by cost-effective laser diodes available on the market, and conventional CMOS-based image sensors have good external quantum efficiencies at its emission wavelengths. The embedded chamber within the tissue phantom is first located, for alignment of the mobile microscope, by filling it with a high-concentration dye solution (~2 μg/mL, *i.e.*, ~ 20,000-fold higher than our detection limit), and it is accordingly positioned to be in the middle of the FOV of the mobile microscope. The chamber is then washed with a continuous flow of DI water (~3 mL) using a syringe pump (Chemyx Fusion 200). After this washing step, the excitation light and the image sensor are turned on. The chamber is then filled with the target concentration of the fluorophore during continuous pumping for 180 s at a flow-rate of 60 μL/min. The dye enters the chamber and into the FOV of our imager at around 90 s and is constantly refreshed until the pumping stops. The fluorescent emission through the skin phantom is continuously imaged by our mobile fluorescence microscope during and after the pumping process for 5 min. The CMOS image sensor chip is set to operate without gain, and the exposure time is set to be 1 s.

**Processing of Fluorescence Microscopy Images.** Figure 2 provides an overview of our algorithm that is used for processing of the acquired fluorescence images. Each captured sequence of images in a given measurement is divided into two subsets. The first 10 frames are used to create an autofluorescence background image by averaging them to reduce noise. This background image is used as a reference for subsequent images acquired during a measurement; for a wearable *in vivo* sensing system, the same background image can be calculated by acquiring images at a sensor-free part of the skin surface with a small lateral offset or alternatively before the activation or implantation of the sensor, as we can assume that the skin does not experience significant changes in its autofluorescence behavior at the selected spot during the operation of the wearable sensing system. To reduce the intensity noise arising from the stability of the laser diode-based excitation, the mean of each image frame is equalized to the background image before subtraction (see Figure 2). As detailed in the Results and Discussion section, the *spatial distribution* of each one of these mean equalized and background subtracted images is strictly related to two simultaneous processes that happen during a fluorescence measurement: (1) the change of the skin's autofluorescence emission distribution due to spatially and temporally varying photobleaching, and (2) the presence of the target fluorescent dye within the embedded sample/sensor volume. The excitation beam profile mainly determines the former, while the latter is influenced by the size, shape, and location of the embedded sample volume containing the target dye. Note that here we ignore any spatial modulation in a fluorescence image that might be introduced by potential photobleaching or degradation of the target fluorescent sample within the skin. As detailed in the Results and Discussion section, this is a reasonable assumption since the width of the implanted target fluorescent volume would be negligible compared to the width of the scattered excitation beam within human skin. This is certainly the case for our phantom experiments where the fluorescent reservoir width is ~0.5 mm, whereas the excitation beam width within the phantom approaches ~1 cm after tissue scattering, even for a smaller phantom depth of 0.5 mm.

In order to separate these two contributions from each other (tissue autofluorescence *vs* target dye fluorescence) and be able to measure the changes in the spatial distribution of our images caused by the presence of the dye in the target sample volume, we take a 2D spatial Fourier transform of each one of the mean equalized and background subtracted frames, as shown in Figure 2. We then locate and measure the amplitude of a spatial frequency (refer to the Results and Discussion section for details) that is linked to the target fluorescent dye volume embedded within the skin phantom and track it as a function of time using our mobile microscope with a frame rate of 1 fps.

Our Results and Discussion section also provides a mathematical analysis of the above outlined image processing flow to shed more light into how it is used to separate the true fluorescent signal that is generated by the target dye volume from tissue autofluorescence.

**Measuring the Lateral Misalignment Tolerance of the Mobile Microscope.** In our experiments, we initially align the sample chamber containing the target dye to be in the middle of the FOV of our mobile microscope. To test misalignment tolerances of this imaging system, the phantom is then laterally shifted using a translation stage along either the major or the minor axis of our elliptical excitation beam profile, which is followed by the same detection/imaging process that is detailed earlier.

## ASSOCIATED CONTENT

### Supporting Information

Supplementary figure. The Supporting Information is available free of charge on the ACS Publications website at DOI: 10.1021/acsnano.6b05129.

Figure of faceplate-based lens-free fluorescent reader configurations (PDF)

## AUTHOR INFORMATION

### Corresponding Author

*E-mail: ozcan@ucla.edu.

### Notes

The authors declare the following competing financial interest(s): An intellectual property application on this work has been filed through UCLA Office of Intellectual Property.

## ACKNOWLEDGMENTS

This project has been supported by Verily Life Sciences, LLC (formerly known as Google Life Sciences). The Ozcan Research Group at UCLA also acknowledges the support of the Presidential Early Career Award for Scientists and Engineers (PECASE), the Army Research Office (ARO; W911NF-13-1-0419 and W911NF-13-1-0197), the ARO Life Sciences Division, the National Science Foundation (NSF) CBET Division Biophotonics Program, the NSF Emerging Frontiers in Research and Innovation (EFRI) Award, the NSF EAGER Award, NSF INSPIRE Award, NSF Partnerships for Innovation: Building Innovation Capacity (PFI:BIC) Program, Office of Naval Research (ONR), the National Institutes of Health (NIH), the Howard Hughes Medical Institute (HHMI), Vodafone Americas Foundation, and KAUST. This work is based upon research performed in a laboratory renovated by the National Science Foundation under grant no. 0963183, which is an award funded under the American Recovery and Reinvestment Act of 2009 (ARRA). Furthermore, Y.R. is supported by the European Union's Horizon 2020 research and innovation program under grant agreement no. H2020-MSCA-IF-2014-659595 (MCMQCT).

## REFERENCES

(1) Ruckh, T. T.; Mehta, A. A.; Dubach, J. M.; Clark, H. A. Polymer-Free Optode Nanosensors for Dynamic, Reversible, and Ratiometric Sodium Imaging in the Physiological Range. *Sci. Rep.* **2013**, *3*, 3366.

(2) Barker, S. L. R.; Clark, H. A.; Swallen, S. F.; Kopelman, R.; Tsang, A. W.; Swanson, J. A. Ratiometric and Fluorescence-Lifetime-Based Biosensors Incorporating Cytochrome c′ and the Detection of Extra- and Intracellular Macrophage Nitric Oxide. *Anal. Chem.* **1999**, *71*, 1767−1772.

(3) Tung, C.-H.; Mahmood, U.; Bredow, S.; Weissleder, R. In Vivo Imaging of Proteolytic Enzyme Activity Using a Novel Molecular Reporter. *Cancer Res.* **2000**, *60*, 4953−4958.



DOI: 10.1021/acsnano.6b05129
*ACS Nano* XXXX, XXX, XXX−XXX

(4) Xing, B.; Khanamiryan, A.; Rao, J. Cell-Permeable Near-Infrared Fluorogenic Substrates for Imaging β-Lactamase Activity. *J. Am. Chem. Soc.* **2005**, *127*, 4158−4159.
(5) Azzazy, H. M. E.; Mansour, M. M. H.; Kazmierczak, S. C. From Diagnostics to Therapy: Prospects of Quantum Dots. *Clin. Biochem.* **2007**, *40*, 917−927.
(6) Dubach, J. M.; Harjes, D. I.; Clark, H. A. Ion-Selective Nano-Optodes Incorporating Quantum Dots. *J. Am. Chem. Soc.* **2007**, *129*, 8418−8419.
(7) Resch-Genger, U.; Grabolle, M.; Cavaliere-Jaricot, S.; Nitschke, R.; Nann, T. Quantum Dots *versus* Organic Dyes as Fluorescent Labels. *Nat. Methods* **2008**, *5*, 763−775.
(8) Wagner, M. K.; Li, F.; Li, J.; Li, X.-F.; Le, X. C. Use of Quantum Dots in the Development of Assays for Cancer Biomarkers. *Anal. Bioanal. Chem.* **2010**, *397*, 3213−3224.
(9) Cash, K. J.; Clark, H. A. Nanosensors and Nanomaterials for Monitoring Glucose in Diabetes. *Trends Mol. Med.* **2010**, *16*, 584−593.
(10) Petryayeva, E.; Algar, W. R.; Medintz, I. L. Quantum Dots in Bioanalysis: A Review of Applications across Various Platforms for Fluorescence Spectroscopy and Imaging. *Appl. Spectrosc.* **2013**, *67*, 215−252.
(11) Wu, L.; Qu, X. Cancer Biomarker Detection: Recent Achievements and Challenges. *Chem. Soc. Rev.* **2015**, *44*, 2963−2997.
(12) Etrych, T.; Lucas, H.; Janoušková, O.; Chytil, P.; Mueller, T.; Mäder, K. Fluorescence Optical Imaging in Anticancer Drug Delivery. *J. Controlled Release* **2016**, *226*, 168−181.
(13) Zelmer, A.; Ward, T. H. Noninvasive Fluorescence Imaging of Small Animals. *J. Microsc.* **2013**, *252*, 8−15.
(14) Popp, J.; Tuchin, V. V.; Chiou, A.; Heinemann, S. H. *Handbook of Biophotonics: Photonics for Health Care*; Wiley-VCH: Weinheim, Germany, 2011; Vol 2.
(15) Stuker, F.; Ripoll, J.; Rudin, M. Fluorescence Molecular Tomography: Principles and Potential for Pharmaceutical Research. *Pharmaceutics* **2011**, *3*, 229−274.
(16) Masters, B. R.; So, P. T.; Gratton, E. Multiphoton Excitation Fluorescence Microscopy and Spectroscopy of *in Vivo* Human Skin. *Biophys. J.* **1997**, *72*, 2405−2412.
(17) Billinton, N.; Knight, A. W. Seeing the Wood through the Trees: A Review of Techniques for Distinguishing Green Fluorescent Protein from Endogenous Autofluorescence. *Anal. Biochem.* **2001**, *291*, 175−197.
(18) Laiho, L. H.; Pelet, S.; Hancewicz, T. M.; Kaplan, P. D.; So, P. T. C. Two-Photon 3-D Mapping of Ex Vivo Human Skin Endogenous Fluorescence Species Based on Fluorescence Emission Spectra. *J. Biomed. Opt.* **2005**, *10*, 024016−02401610.
(19) Bradley, R. S.; Thorniley, M. S. A Review of Attenuation Correction Techniques for Tissue Fluorescence. *J. R. Soc., Interface* **2006**, *3*, 1−13.
(20) Weersink, R.; Patterson, M. S.; Diamond, K.; Silver, S.; Padgett, N. Noninvasive Measurement of Fluorophore Concentration in Turbid Media with a Simple Fluorescence/reflectance Ratio Technique. *Appl. Opt.* **2001**, *40*, 6389.
(21) Pogue, B. W.; Hasan, T. Fluorophore Quantitation in Tissue-Simulating Media with Confocal Detection. *IEEE J. Sel. Top. Quantum Electron.* **1996**, *2*, 959−964.
(22) Biswal, N.; Gupta, S.; Ghosh, N.; Pradhan, A. Recovery of Turbidity Free Fluorescence from Measured Fluorescence: An Experimental Approach. *Opt. Express* **2003**, *11*, 3320.
(23) Chen, Y.; Chen, Z.-P.; Yang, J.; Jin, J.-W.; Zhang, J.; Yu, R.-Q. Quantitative Fluorescence Spectroscopy in Turbid Media: A Practical Solution to the Problem of Scattering and Absorption. *Anal. Chem.* **2013**, *85*, 2015−2020.
(24) Durkin, A. J.; Jaikumar, S.; Ramanujam, N.; Richards-Kortum, R. Relation between Fluorescence Spectra of Dilute and Turbid Samples. *Appl. Opt.* **1994**, *33*, 414.
(25) Welch, A. J.; Gardner, C.; Richards-Kortum, R.; Chan, E.; Criswell, G.; Pfefer, J.; Warren, S. Propagation of Fluorescent Light. *Lasers Surg. Med.* **1997**, *21*, 166−178.
(26) Zeng, H.; MacAulay, C.; McLean, D. I.; Palcic, B. Spectroscopic and Microscopic Characteristics of Human Skin Autofluorescence Emission. *Photochem. Photobiol.* **1995**, *61*, 639−645.
(27) Chen, J.; Zhuo, S.; Luo, T.; Jiang, X.; Zhao, J. Spectral Characteristics of Autofluorescence and Second Harmonic Generation from Ex Vivo Human Skin Induced by Femtosecond Laser and Visible Lasers. *Scanning* **2006**, *28*, 319−326.
(28) Rice, W. L.; Shcherbakova, D. M.; Verkusha, V. V.; Kumar, A. T. N. In Vivo Tomographic Imaging of Deep Seated Cancer Using Fluorescence Lifetime Contrast. *Cancer Res.* **2015**, *75*, 1236−1243.
(29) Hu, C.; Zhao, Y.; Qin, B. Spectral Unmixing for *in Vivo* Fluorescence Imaging Based on Accurate Target-to-Background Estimation. Proceedings of the *2013 IEEE Nuclear Science Symposium and Medical Imaging Conference (2013 NSS/MIC)*, Seoul, Korea, October 26−November 2, 2013; IEEE: New York, 2013; pp 1−4.
(30) Huang, S.; Zhao, Y.; Hu, C.; Qin, B. Nonnegative Matrix Factorization Using Target-to-Background Contrast for Fluorescence Unmixing. Proceedings of the *2013 IEEE International Conference on Medical Imaging Physics and Engineering (ICMIPE)*, Shenyang, China, October 19−20, 2013; IEEE: New York, 2013; pp 287−292.
(31) Troy, T.; Jekic-McMullen, D.; Sambucetti, L.; Rice, B. Quantitative Comparison of the Sensitivity of Detection of Fluorescent and Bioluminescent Reporters in Animal Models. *Mol. Imaging* **2004**, *3*, 9−23.
(32) Ozcan, A. Mobile Phones Democratize and Cultivate next-Generation Imaging, Diagnostics and Measurement Tools. *Lab Chip* **2014**, *14*, 3187−3194.
(33) Ozcan, A.; McLeod, E. Lensless Imaging and Sensing. *Annu. Rev. Biomed. Eng.* **2016**, *18*.7710210.1146/annurev-bioeng-092515-010849
(34) Ludwig, S. K. J.; Zhu, H.; Phillips, S.; Shiledar, A.; Feng, S.; Tseng, D.; van Ginkel, L. A.; Nielen, M. W. F.; Ozcan, A. Cellphone-Based Detection Platform for rbST Biomarker Analysis in Milk Extracts Using a Microsphere Fluorescence Immunoassay. *Anal. Bioanal. Chem.* **2014**, *406*, 6857−6866.
(35) Wei, Q.; Qi, H.; Luo, W.; Tseng, D.; Ki, S. J.; Wan, Z.; Göröcs, Z.; Bentolila, L. A.; Wu, T.-T.; Sun, R.; Ozcan, A. Fluorescent Imaging of Single Nanoparticles and Viruses on a Smart Phone. *ACS Nano* **2013**, *7*, 9147−9155.
(36) Zhu, H.; Mavandadi, S.; Coskun, A. F.; Yaglidere, O.; Ozcan, A. Optofluidic Fluorescent Imaging Cytometry on a Cell Phone. *Anal. Chem.* **2011**, *83*, 6641−6647.
(37) Ghauharali, R. I.; Brakenhoff, G. J. Fluorescence Photobleaching-Based Image Standardization for Fluorescence Microscopy. *J. Microsc.* **2000**, *198*, 88−100.
(38) Berglund, A. J. Nonexponential Statistics of Fluorescence Photobleaching. *J. Chem. Phys.* **2004**, *121*, 2899−2903.
(39) Goodman, J. W. *Statistical Optics*; 1 ed.; Wiley-Interscience: New York, 2000.
(40) Greenbaum, A.; Luo, W.; Su, T.-W.; Göröcs, Z.; Xue, L.; Isikman, S. O.; Coskun, A. F.; Mudanyali, O.; Ozcan, A. Imaging without Lenses: Achievements and Remaining Challenges of Wide-Field on-Chip Microscopy. *Nat. Methods* **2012**, *9*, 889−895.
(41) Greenbaum, A.; Zhang, Y.; Feizi, A.; Chung, P.-L.; Luo, W.; Kandukuri, S. R.; Ozcan, A. Wide-Field Computational Imaging of Pathology Slides Using Lens-Free on-Chip Microscopy. *Sci. Transl. Med.* **2014**, *6*, 267ra175−267ra175.
(42) Coskun, A. F.; Sencan, I.; Su, T.-W.; Ozcan, A. Wide-Field Lensless Fluorescent Microscopy Using a Tapered Fiber-Optic Faceplate on a Chip. *Analyst* **2011**, *136*, 3512−3518.
(43) Coskun, A. F.; Sencan, I.; Su, T.-W.; Ozcan, A. Lensfree Fluorescent On-Chip Imaging of Transgenic Caenorhabditis Elegans Over an Ultra-Wide Field-of-View. *PLoS One* **2011**, *6*, e15955.
(44) Coskun, A. F.; Sencan, I.; Su, T.-W.; Ozcan, A. Lensless Wide-Field Fluorescent Imaging on a Chip Using Compressive Decoding of Sparse Objects. *Opt. Express* **2010**, *18*, 10510−10523.
(45) *ANSI Z136. 1 Safe Use of Lasers (2014)*; Laser Institute of America: Orlando, FL, 2014.


DOI: 10.1021/acsnano.6b05129
*ACS Nano* XXXX, XXX, XXX−XXX

(46) Tseng, S.-H.; Grant, A.; Durkin, A. J. In Vivo Determination of Skin near-Infrared Optical Properties Using Diffuse Optical Spectroscopy. *J. Biomed. Opt.* **2008**, *13*, 014016.
(47) Baeten, J.; Niedre, M.; Dunham, J.; Ntziachristos, V. Development of Fluorescent Materials for Diffuse Fluorescence Tomography Standards and Phantoms. *Opt. Express* **2007**, *15*, 8681−8694.
(48) Pickering, J. W.; Prahl, S. A.; van Wieringen, N.; Beek, J. F.; Sterenborg, H. J. C. M.; van Gemert, M. J. C. Double-Integrating-Sphere System for Measuring the Optical Properties of Tissue. *Appl. Opt.* **1993**, *32*, 399−410.
(49) Prahl, S. A.; van Gemert, M. J. C.; Welch, A. J. Determining the Optical Properties of Turbid Media by Using the Adding−doubling Method. *Appl. Opt.* **1993**, *32*, 559−568.
(50) *Absorption and Scattering of Light by Small Particles*; Bohren, C. F., Huffman, D. R., Eds.; Wiley-VCH Verlag GmbH: Weinheim, Germany, 1998.



DOI: 10.1021/acsnano.6b05129
*ACS Nano* XXXX, XXX, XXX−XXX